

<https://doi.org/10.1038/s43246-025-00782-7>

# Homogeneous spin-dephasing time of NV<sup>-</sup> centre in millimetre-scale <sup>12</sup>C-enriched high-pressure high-temperature diamond crystals

Check for updates

Chikara Shinei<sup>1,2</sup>✉, Yuta Masuyama<sup>3</sup>, Hiroshi Abe<sup>3</sup>, Masashi Miyakawa<sup>1</sup>, Takashi Taniguchi<sup>1</sup>, Takeshi Ohshima<sup>3</sup> & Tokuyuki Teraji<sup>1</sup>✉

Negatively charged nitrogen vacancy (NV<sup>-</sup>) centres in diamond crystals are promising colour centres for high-sensitivity quantum sensors. A long dephasing time ( $T_2^* > 10 \mu\text{s}$ ) is essential for achieving increased sensitivity and higher uniformity of  $T_2^*$  in millimetre-scale diamond is strongly desired for femto-tesla weak magnetic field detection. High uniformity of  $T_2^*$  for NV<sup>-</sup> centres is achieved herein. The median value of  $T_2^*$ ,  $\langle T_2^* \rangle$ , in the <sup>12</sup>C-enriched high-pressure, high-temperature (HPHT) grown diamond with a nitrogen concentration of  $1.3 \pm 0.4 \text{ ppm}$  is  $4.5 \mu\text{s}$ . The variance of  $T_2^*$  is only 10% over a millimetre-scale region ( $1.1 \times 1.1 \text{ mm}^2$ ) within the 0.4 mm thick {111} growth sector.  $\langle T_2^* \rangle$  is  $\sim 2/3$  times the value limited by the dipole-dipole interaction from the electron-spin bath of nitrogen impurities, suggesting that the residual strain gradient in the HPHT diamond crystal partially limits  $T_2^*$ . Reducing the strain gradient in diamond crystals provide a pathway to achievement of high sensitivity magnetometry using NV quantum sensing.

The quantum superposition states (QSS) of electron and nuclear spins in point defects in wide-gap semiconductors are stable at room temperature<sup>1</sup>. These superposition states in semiconductors can prospectively be used for various quantum applications such as quantum computation<sup>2</sup>, and quantum sensing<sup>1,3,4</sup>. In quantum sensing, a type of quantum technology, the magnitude of external fields such as magnetic fields, electric fields, and temperature are measured by detecting phase changes of the QSS. In general, QSS reflecting quantum effects are expected to provide higher-sensitivity measurements than classical sensing<sup>1</sup>. To achieve higher sensitivity in quantum sensing using QSS, extending both the number of sensors and the spin-dephasing time,  $T_2^*$ , are essential.

The QSS of the electron spins of NV<sup>-</sup> centres formed in diamond are attractive quantum systems because the ensemble of electron spins has an extremely long  $T_2^*$  of tens of microseconds at room temperature<sup>5</sup>. For NV<sup>-</sup> centres,  $T_2^*$  is relatively long even at room temperature because of the extremely small nuclear spin concentration of 1.1% in diamond<sup>6,7</sup>. The value of  $T_2^*$  has been extended using <sup>12</sup>C isotopically enriched diamond with [<sup>13</sup>C] <500 ppm<sup>8-10</sup>, and a quantum sensor for measuring weak magnetic fields has been demonstrated using optically excited NV<sup>-</sup> centres created in <sup>12</sup>C-enriched diamond<sup>11</sup>. In addition to the elongation  $T_2^*$  of the NV<sup>-</sup> centre,

the crystal size of optically excited diamond, which determines the total number of excited NV<sup>-</sup> centres, must be enlarged to achieve high magnetic sensitivity. In recent research<sup>12</sup>, a minimum detectable magnetic field sensitivity (MDMFS) of  $9.4 \text{ pT Hz}^{-1/2}$  was reported in a relatively small excitation volume of  $0.004 \text{ mm}^3$ . This sensitivity was the best reported value in the DC frequency range of 5–100 Hz. In the previous report, a long  $T_2^*$  of the NV<sup>-</sup> centre ensemble ( $\sim 2 \mu\text{s}$ ) was achieved by <sup>12</sup>C isotopic enrichment. The achieved sensitivity corresponds to the shot noise limit, which is a quantum-limiting MDMFS. The long  $T_2^*$  and reduction in PL intensity noise by laser mainly contributed for the achieved the best reported sensitivity. Here, we proposed that enlargement of the reported excitation volume:  $0.004 \text{ mm}^3$  could lead to higher sensitivity while maintaining the factors contributing to the best reported sensitivity; long  $T_2^*$  ( $\sim 2 \mu\text{s}$ ) and PL intensity noise cancelling. Arai et al. reported a relatively large excitation diamond crystal volume of  $0.19 \text{ mm}^3$  for NV sensing<sup>13</sup>. The excitation volume was achieved by laser beam spot size being  $\sim 0.4 \text{ mm}$  in diameter with high laser power (2 W) and constructing a reflection pass of excitation laser in a diamond crystal<sup>13</sup>. Here, the increase in excitation volume contributes to improve the shot noise limit<sup>1</sup>. Based on the relationship that the shot-noise limit theoretically improves by a factor of the square root of the excitation volume

<sup>1</sup>National Institute for Materials Science, Tsukuba, Ibaraki, 3050044, Japan. <sup>2</sup>University of Tsukuba, Tsukuba, Ibaraki, 3058577, Japan. <sup>3</sup>National Institutes for Quantum Science and Technology, Takasaki, Gunma, 3701292, Japan. ✉e-mail: [shinei.chikara.fb@u.tsukuba.ac.jp](mailto:shinei.chikara.fb@u.tsukuba.ac.jp); [TERAJI.Tokuyuki@nims.go.jp](mailto:TERAJI.Tokuyuki@nims.go.jp)

increase rate, NV sensing using the reported large excitation volume of 0.19 mm<sup>3</sup> with high laser power and NV<sup>-</sup> centre with a long  $T_2^*$  of ~ 2 μs could lead to higher magnetic sensitivity (<1 pT Hz<sup>-1/2</sup>). There are several factors that substantially reduce magnetic sensitivity when the excitation volume is increased. One of them is significant increase of PL intensity noise due to larger laser power. To increase the excitation volume while maintaining the higher emission rate of each NV<sup>-</sup> centre, the laser power has to be increased. The PL intensity noise by high laser power is expected to be cancelled by a balanced photon detection technique<sup>12,13</sup>. Another is the strain distribution, which becomes more pronounced as the excitation volume increases. The estimation of the improvement in sensitivity due to the increase in the excitation volume was based on a condition that the NV centres in the increased excitation volume have a long  $T_2^*$  with uniformed spatial distribution. Here, imperfection of diamond crystal such as strain inhomogeneities<sup>1</sup> and magnetic noise by spin bath<sup>1</sup> cause shorten of  $T_2^*$ . For example, defects such as dislocations and plastic deformation defects distributed over sub-millimetre-sized areas are formed during the synthesis of diamonds with millimetre-sized volumes<sup>14</sup>. These defects cause inhomogeneous strain distribution and reduce the  $T_2^*$  of the NV<sup>-</sup> centre in the excitation volume<sup>14</sup>. Therefore, we concluded that increasing the excitation volume and spatial homogeneity of  $T_2^*$  by reducing the imperfection of diamond crystal in the excitation volume at the same time would be the key to constructing highly sensitive magnetometers.

For example, the achievement of human magnetoencephalography under ambient conditions is a major milestone in quantum sensing using a NV<sup>-</sup> centres<sup>12</sup>. An MDMFS of less than 10 fT<sup>15</sup> is required for human magnetoencephalography measurements. Herein, the crystal size needed to obtain a sensitivity of 10 fT is estimated. The sensitivity is expressed as the DC shot noise limit ( $\eta_{sp}^{ensemble}$ ) as represented by Eq. 1<sup>13</sup>,

$$\eta_{sp}^{ensemble} = \frac{1}{\gamma_{NV}} \frac{1}{C \times n_{avg}} \frac{1}{\sqrt{\beta} \sqrt{V \times [NV^-]} \times T_2^*} \quad (1)$$

$\gamma_{NV}$ ,  $C$ ,  $n_{avg}$ ,  $\beta$  and  $V$  are gyromagnetic ratio of the NV<sup>-</sup> centre spin of  $1.76 \times 10^{11}$  Hz T<sup>-1</sup>, the spin-dependent NV<sup>-</sup> centre PL contrast, average number of photons collected per NV<sup>-</sup> centre per measurement, photon collection efficiency, and excitation diamond crystal volume, respectively. The product of  $V$  and  $[NV^-]$  represents the total number of NV<sup>-</sup> centres in the excitation volume of the diamond crystal. The concentration of NV<sup>-</sup> centres is typically limited by the total nitrogen concentration in the diamond. The reported maximum efficiency for the conversion of nitrogen to NV<sup>-</sup> centres is about 50%<sup>16,17</sup>. The  $T_2^*$  value of the NV<sup>-</sup> centre ensemble was limited by the total nitrogen concentration when the <sup>13</sup>C concentration and strain spatial distribution were significantly small<sup>18</sup>.  $T_2^*$  was found to be inversely proportional to the total nitrogen concentration, with an inverse coefficient of 9.9 μs ppm (corresponding to dephasing rate per density: 101 kHz ppm<sup>-1</sup>)<sup>10</sup>. Using the maximum conversion efficiency  $[NV^-]/[N]$  of 0.5 and the  $T_2^*$  value limited by the total nitrogen concentration expressed as 9.9/[N], the shot noise limit equation (Eq. 1) can be transformed to Eq. 2.

$$\eta_{sp}^{ensemble} = \frac{1}{\gamma_{NV}} \frac{1}{C \times n_{avg}} \frac{1}{\sqrt{\beta} \sqrt{V \times 0.5 \times 9.9}} \quad (2)$$

The product of the PL contrast and square root of the average photon counts of the NV<sup>-</sup> centre ensemble shown in Eq. 2,  $C \times n_{avg}^{1/2}$  is an indicator of the photon readout fidelity for the NV<sup>-</sup> centre. This readout fidelity is unity under ideal condition, which is the spin projection limiting value<sup>1</sup>. However, in the typical photon readout fidelity for NV<sup>-</sup> centres,  $C \times n_{avg}^{1/2}$  was reported to have a significant lower value 1/5000-1/1000<sup>1</sup> than the spin projection limiting value. By using the total reflection of the photon emission of the NV<sup>-</sup> centre in diamond, a value of 1/67 as  $C \times n_{avg}^{1/2}$  was achieved<sup>19</sup>, which is two orders of magnitude larger than the typical reported values. This two-magnitude improvement in the photon readout fidelity contributed to enhancing the magnetic sensitivity<sup>19</sup>. For the excitation of millimetre-sized diamond volumes, this total internal reflection method is

thought to be essential. And photon collection efficiency can be improved to 65% by using a trapezoidal-cut diamond crystal and a parabolic concentrator<sup>20</sup>. Using the shot noise limits in Eq. 2 with photonic parameters as  $C \times n_{avg}^{1/2} = 1/67$  and  $\beta = 0.65$ , to achieve a magnetic sensitivity below 10 fT, the minimum excitation diamond volume  $V$  was estimated to be ~ 2.6 mm<sup>3</sup>.

The estimation of the minimum excitation diamond volume for human magnetoencephalography using the shot noise limit equation does not consider high-fidelity spin-rotation operations for high-precision quantum sensing. During quantum sensing, the protocol of spin half-rotation in a Bloch sphere is essential for preparing QSS. The phase of the QSS fluctuates when the half  $\pi$ -rotation time ( $T_\pi/2$ ), that is, the generation time of the QSS, is significantly larger than the spin-dephasing time,  $T_2^*$ . To avoid phase fluctuation, in general,  $T_\pi/2$  must be set to a value significantly shorter than  $T_2^*$ . This criterion suggests that the spin rotation is completed well before phase coherence is lost. In order to perform high-fidelity spin rotation, the value of  $T_2^*$  needs to be over two orders of magnitude longer than  $T_\pi$ <sup>21</sup>. For achieving high sensitivity using NV sensing, so far, some previous reports showed spin  $\pi$ -rotation time of ~ 50 ns<sup>22</sup> and ~ 100 ns<sup>23,24</sup>. Because the spin  $\pi$ -rotation time of the NV<sup>-</sup> centre in this study is approximately 100 ns, the minimum spin-dephasing time required for high-fidelity spin rotation is estimated to be 10 μs. To achieve a  $\pi$  rotation time of ~ 100 ns, a driving microwave (MW) magnetic field amplitude of 0.18 ~ 0.21 mT<sup>23,24</sup> was applied to the NV<sup>-</sup> centre ensemble. The spin-rotation time is determined by the strength of the microwave magnetic field applied to the NV<sup>-</sup> centre. The larger the amplitude of the microwave magnetic field applied to the NV<sup>-</sup> centre, the faster the spin rotation is. A  $T_2^*$  of over 10 μs is expected when the total nitrogen concentration is below 1 ppm because the total nitrogen concentration and  $T_2^*$  are inversely proportional in this nitrogen doping range. From the shot noise limit and criteria for high-fidelity spin rotation, millimetre-sized diamond crystals and  $T_2^* > 10 \mu s$  are essential for 10 fT human magnetoencephalography.

Previous research has been conducted using diamonds synthesised by chemical vapour deposition (CVD), a common diamond growth method, to increase the  $T_2^*$  of NV<sup>-</sup> centres formed in millimetre-sized diamond single crystals and improve their spatial uniformity. Indeed,  $T_2^*$  spatial mapping has reportedly been carried out within an area of 1 mm × 1 mm in the {001} plane of 0.1 μm thick diamond, where non-uniform  $T_2^*$  spatial distribution was observed<sup>18</sup>. In that study, the  $T_2^*$  inhomogeneity was caused by a strain gradient in the diamond crystal. One of the factors contributing to the spatial distribution of strain in CVD diamonds is the dislocation distribution. In a previous report, high-density dislocation distributions ranging from 10<sup>4</sup> to 10<sup>6</sup> cm<sup>-2</sup> were observed in CVD diamond crystals using X-ray topography<sup>25</sup>. Furthermore, Kehayias et al. reported the distribution of NV<sup>-</sup> centres with a short and non-uniform  $T_2^*$  in the dislocation area in CVD diamond crystals<sup>14</sup>. High-pressure, high-temperature (HPHT) synthesis is another common method for diamond growth. In the HPHT method, diamond is synthesised under equilibrium conditions; therefore, it is thought that the formation of high-density dislocation defects as observed in CVD diamond is unlikely, as there have been reports of millimetre-sized HPHT diamond single crystals with low dislocation densities of less than 10<sup>2</sup> cm<sup>-2</sup><sup>26,27</sup>. Therefore, NV<sup>-</sup> centres with a uniformly distributed, long  $T_2^*$  are expected to be obtained in HPHT nitrogen-doped diamonds. In previous report, strain imaging by NV sensing were carried out with millimetre-sized nitrogen doped CVD diamond<sup>18</sup>. The imaging cross-sectional area was 1 mm<sup>2</sup> and the doped nitrogen concentration was 0.75 ppm. The obtained strain imaging indicated partial sub-millimetre-sized large strain distributions. This sub-millimetre-sized distribution caused degradation of  $T_2^*$  and a significant large variation of  $T_2^*$  (1-10 μs) was also reported in that previous study. The large variation of  $T_2^*$  could cause degradation of the averaged  $T_2^*$  in excited millimetre-sized diamond crystal volume. Therefore, expected millimetre-sized homogeneous  $T_2^*$  distribution in HPHT diamond crystal is essential for human magnetoencephalography.

In this study, low-strain, nitrogen-doped diamond crystals are synthesised using HPHT synthesis method. These low-strain HPHT diamond

crystals are used for millimetre-size  $T_2^*$  imaging and to clarify the millimetre-size distributed dephasing factor of  $NV^-$  centre spin coherence. Finally, high uniformity of the spin dephasing time of  $NV^-$  centres in millimetre-scale area was achieved using  $^{12}C$ -enriched nitrogen doped HPHT diamond crystals, and in region of nitrogen impurity concentrations less than  $\sim 1$  ppm, it was found that the strain gradient in HPHT diamond crystals partially limits spin dephasing time.

## Results and discussion

### Synthesis of HPHT diamond crystals

In order to form an ensemble of  $NV^-$  centres that contributes to magnetoencephalography, it is necessary to extend  $T_2^*$  to over 10  $\mu s$ . To achieve this, the density of the doped nitrogen must be controlled, and the nitrogen concentration should be reduced to less than 1 ppm. In general, the nitrogen concentration can be controlled by adding nitrogen-getter metals such as Ti and Al to the solvent-metal during HPHT synthesis. The nitrogen-getter metal and solvent-metal are described in the sample preparation of Methods section. Precise nitrogen concentration control ranging from 0.2 to 100 ppm was achieved by controlling the amount of the nitrogen-getter metal<sup>28</sup>. During HPHT synthesis of diamond, when the growth rate was higher than  $6\text{--}7\text{ mg h}^{-1}$ , the solvent-metal used in HPHT synthesis was incorporated into the growing diamond, resulting in the formation of metal inclusions<sup>29</sup>. These metal inclusions become a source of strain gradients distributed over millimetre-sized areas. To suppress the formation of metal inclusions and synthesis large diamond crystal, the lower growth rate than  $6\text{--}7\text{ mg h}^{-1}$  and long growth time: over several tens of hours are required<sup>29</sup>. When growing diamond crystals for a long time to obtain high-quality crystals, changes in growth rate due to temperature fluctuations can be a problem. To avoid the temperature fluctuation, a modified belt-type, high-pressure apparatus was used<sup>28,30,31</sup>, in which cooling water was available for temperature stabilisation. In this study, HPHT diamond crystals were synthesised using a modified belt-type, high-pressure apparatus, in the temperature range of  $1300\text{--}1350\text{ }^\circ\text{C}$ . The temperature fluctuation was less than  $\pm 7.5\text{ }^\circ\text{C}$ . The growth time and growth rate were  $40\text{--}80\text{ h}$  and  $\sim 1\text{ mg h}^{-1}$ , respectively in this study.

### Sequence of $T_2^*$ spatial mapping for $NV^-$ centres

$T_2^*$  was measured in the millimetre-scale region of the diamond. A columnar excitation fluorescence microscope<sup>23</sup> was used to excite the  $NV^-$  centres throughout the thickness direction of the diamond crystal, which is typically  $400\text{ }\mu\text{m}$ . Because the  $532\text{ nm}$  laser diameter and depth of the excitation region in the employed microscope are designed to be  $20$  and  $500\text{ }\mu\text{m}^2$ , respectively, the ensemble of  $NV^-$  centres was excited at the same time, as shown in Fig. 1a. The spatial distribution of  $T_2^*$  in the  $\{111\}$  plane was evaluated as follows: (1) Optically detected magnetic resonance (ODMR) measurements were performed at each excited position. During the measurements, an external magnetic field of  $2.5\text{ mT}$  was applied along the direction of the  $[111]$  diamond crystal. The obtained ODMR frequency was generally  $\sim 2.8\text{ GHz}$ . (2) Subsequently, spatial Rabi measurements were performed at the same excited position. The MW frequency was set to the ODMR frequency obtained at the same excited position. The typical duration of the microwave  $\pi/2$  pulse in the Rabi oscillation was  $\sim 50\text{ ns}$ . (3) Finally, free-induction decay (FID) measurements were performed at the same excited position, where the duration of the microwave  $\pi/2$  pulse was obtained from Rabi measurement at the same excited position. A typical FID signal was shown in Fig. 1c.  $T_2^*$  was estimated by fitting the obtained FID signal to the damped oscillation function<sup>18</sup>, shown in Eq. 3:

$$S_{\text{FID}}(\tau) = \exp\left(-\frac{\tau}{T_2^*}\right) \sum_{i=1,2,3} A_i \sin(2\pi f_i + \delta_i) \quad (3)$$

where  $f_1, f_2$  and  $f_3$  are the frequencies of the hyperfine splitting magnetic field due to the  $^{14}\text{N}$  atom in the  $NV^-$  centres. The typical values of  $f_1, f_2$  and  $f_3$  are  $0.9, 3$  and  $6\text{ MHz}$ , respectively.

As shown in Fig. 1b, the distance between each laser excited position was set to  $100\text{ }\mu\text{m}$  for  $T_2^*$  spatial mapping within the millimetre-scale  $\{111\}$  growth sector.

### $T_2^*$ spatial mapping in the millimetre-scale $\{111\}$ plane

Figure 1d shows the PL intensity imaging for the  $NV^-$  centre in the HPHT diamond with  $[N_{\text{C}}^0]_{\text{initial}} = 1.3\text{ ppm}$ . The HPHT diamond crystal has flat-areas indicated as Fig. 1d-i, ii, and also has tapered-area indicated as Fig. 1d-iii. The growth sector indicated as Fig. 1d-i including the red square area ( $1.1\text{ mm} \times 1.1\text{ mm}$  for  $T_2^*$  spatial mapping below) was primarily the  $\{111\}$  growth sector. In this red square area, the distribution of PL intensity was nearly homogeneous, and the PL intensity was significantly larger than that of the other growth sectors as indicated in Fig. 1d-ii except for growth sectors in tapered-area as indicated in Fig. 1d-iii. From the relationship between the reported uptake of nitrogen for different growth sectors<sup>32</sup> and the obtained PL intensity from the growth sector in Fig. 1d-ii was  $\{110\}$  or  $\{113\}$  growth sector. The details for PL intensity in multi-growth sectors in flat-areas and the relationship between PL intensity and growth sector in the tapered area were explained in PL intensity of  $NV^-$  centres in multi-growth sectors of Methods section.

Next,  $T_2^*$  spatial mapping was performed in the millimetre-scale  $\{111\}$  plane region of the red square ( $1.1\text{ mm} \times 1.1\text{ mm}$ ) in Fig. 1d. Figure 1e shows the  $T_2^*$  spatial distribution in this  $1.1\text{ mm} \times 1.1\text{ mm}$  region.  $T_2^*$  presented here is the average value of four  $T_2^*$  measurements at the same position (for details, see the Supplementary Note 1). No significant low  $T_2^*$  region was detected in the mapped millimetre-scale area shown in Fig. 1e. This means that the number of millimetre-scale structural defects, such as dislocation bundles and plastic deformation zones observed by Kehayias et al.<sup>14</sup>, is quite small in the millimetre-scale  $\{111\}$  growth sector of the present specimens. On the surface of a diamond crystal, ubiquitous defects cause magnetic noise at the  $NV^-$  centre located within  $100\text{ nm}$  of the surface<sup>33</sup>. In the present study, most of the detected  $NV^-$  centres were located inside the diamond crystal with  $\sim 400\text{ }\mu\text{m}$  thickness, far away from the surface. Therefore, the degradation of the examined  $T_2^*$  caused by the surface magnetic noise was neglected in this study. PL intensity imaging can provide information on the distribution of non-radiative defects near the  $NV^-$  centre because  $NV^-$  photons are transferred from the excited-state level of the  $NV^-$  centre to the non-radiative defect level. This photon transfer caused by non-radiative defects leads to a decrease in the PL intensity. In addition, non-radiative defects may shorten  $T_2^*$  of the  $NV^-$  centre due to magnetic noise or lattice strain from these defects. The PL imaging of  $\{111\}$  growth sector as indicated red square in Fig. 1d showed no area with significantly low PL intensity, demonstrating that the distribution of high-density, non-radiative defects was negligible. Furthermore, there was no obvious correlation between the PL intensity and  $T_2^*$  image in the  $\{111\}$  growth sector, as shown in Fig. 1d and e. This result suggests that non-radiative defects primarily do not limit the  $T_2^*$  distribution in the  $\{111\}$  sector. Birefringence imaging detects microdefects such as dislocations and dislocation bundles. The birefringence imaging in the  $\{111\}$  growth sector is presented in Supplementary Note 2. In birefringence imaging, the distributions of dislocations and dislocation bundles cannot be resolved. This birefringence image also shows that the examined HPHT diamond crystal has high crystallinity (see Supplementary Note 2). Figure 1f shows a histogram of  $T_2^*$  obtained from  $T_2^*$  spatial mapping in the millimetre-scale  $\{111\}$  growth sector. The solid line represents the Gaussian curve fitted to the histogram. The median  $\langle T_2^* \rangle$  of this Gaussian distribution was  $4.5\text{ }\mu\text{s}$ , with a standard deviation of less than 10% of  $\langle T_2^* \rangle$ . The 10% variation in  $T_2^*$  indicates that the HPHT diamond used in this study has a highly uniform spatial distribution of  $T_2^*$ . The obtained spatial variation in  $T_2^*$  was significantly smaller than the previously reported  $T_2^*$  variation of 35%. The reported variation was obtained by  $T_2^*$  mapping in  $150\text{ }\mu\text{m} \times 150\text{ }\mu\text{m}$  region in  $\{001\}$  plane of CVD diamond with  $[N_{\text{r}}] \sim 20\text{ ppm}$ <sup>34</sup>.

The phase of the QSS of the  $NV^-$  centre fluctuates owing to the dipole-dipole interaction (DDI) from the electron-spin bath of nitrogen impurities<sup>1,10,18</sup>. The fluctuation of the QSS phase led to a decrease in  $T_2^*$ .

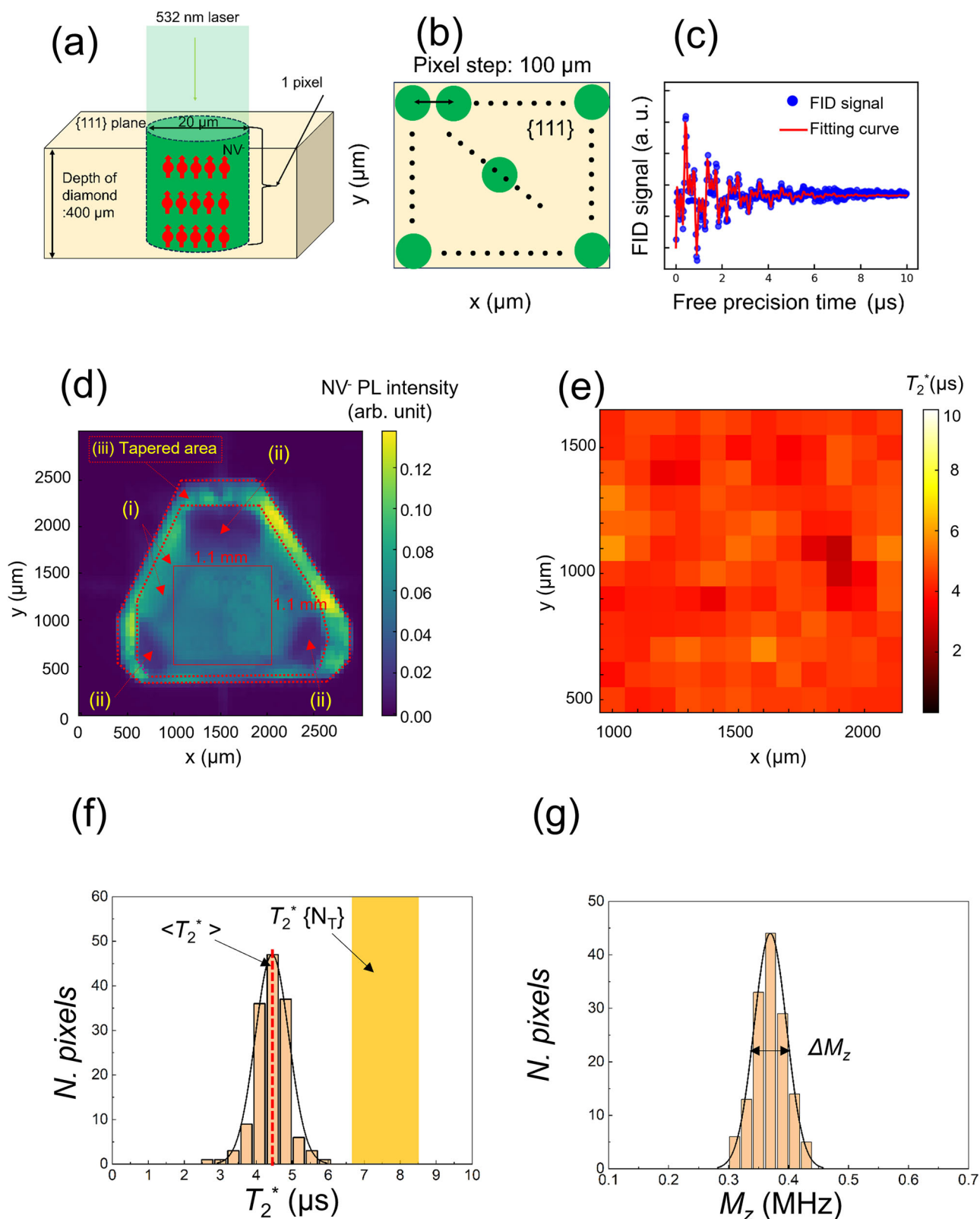


**Fig. 1 |  $T_2^*$  spatial mapping in {111} plane of diamond using columnar excitation fluorescence microscope.** **a** 532 nm laser excitation volume in diamond for one excited position using columnar excitation fluorescence microscope. **b** Schematic of spatial  $T_2^*$  mapping in {111} plane of diamond. **c** Circle symbol indicates representative FID signal respective to free precision time and solid line shows damping oscillation curve as per Eq. 3 for fitting the FID signal. **d** Spatial distribution of PL intensity of NV<sup>-</sup> centre mapped in {111} plane of diamond crystal. Red square region

indicated as (i) shows {111} growth sector in diamond crystal. The lower PL intensity area indicated as (ii) was the {110} or {113} growth sector. The tapered area indicated as (iii) was {110} or {113} growth sector. **e** Spatial  $T_2^*$  mapping in {111} growth sector within the red square (1.1 mm  $\times$  1.1 mm) as shown in this figure. **f** Histogram of  $T_2^*$  from spatial  $T_2^*$  mapping in {111} growth sector of diamond, as shown in this figure. **g** Histogram of  $M_z$  obtained from spatial  $M_z$  mapping in {111} growth sector, as shown in this figure.  $\Delta M_z$  represents FWHM of  $M_z$ .

This phenomenon becomes dominant when the nitrogen concentration exceeds 1 ppm. The spin-dephasing rate,  $1/T_2^*\{N_T\}$ , due to this DDI from the electron-bath of nitrogen impurities is described as follows:

$$\frac{1}{T_2^*\{N_T\}} = D_{N_T} \times [N_T] \quad (4)$$

where  $D_{N_T} = 101 \pm 12 \text{ms}^{-1} \text{ppm}^{-1}$  and  $[N_T]$  is the total concentration of nitrogen impurities in the diamond. The experimentally obtained  $\langle T_2^* \rangle$  was  $4.5 \mu\text{s}$  which is smaller than  $T_2^*\{N_T\} = 7.6 \pm 0.9 \mu\text{s}$  estimated from Eq. 4 with  $[N_T] = [N_s^0]_{\text{initial}} = 1.3 \pm 0.4 \text{ppm}$  for the examined HPHT diamond sample, as seen in the filled orange area in Fig. 1f. This result indicates that the dephasing rate for  $T_2^*$  is affected by sources other than the electron-spin bath of nitrogen impurities. Previous studies reported that the strain gradient in diamond crystals reduces  $T_2^*$  through the interaction between the electronic dipole and the electron spin of the  $NV^-$  centre<sup>14,35</sup>. The dephasing rate due to this strain gradient, which is termed  $1/T_2^*\{\text{strain gradient}\}$  in this study, corresponds to the spatial dispersion of the interaction  $M_z$  between the electron spins and diamond crystal strain. In general,  $M_z$  is one component of the ODMR resonance frequency ( $f_{\pm}$ ) of the  $NV^-$  centre (Eq. 5).

$$f_{\pm} = D + M_z \pm \gamma_{NV} B_z \quad (5)$$

$f_{\pm}$  is composed of the zero-field splitting ( $D$ ) of the electron spin ( $S = 1$ ) of the  $NV^-$  centre, the spin-strain interaction ( $M_z$ ), and the Zeeman splitting caused by the external magnetic field ( $B_z$ )<sup>18,35</sup>. Strain gradients in diamond crystals have been observed as resonance frequency shifts in ODMR<sup>14,35</sup>. In this study,  $M_z$  was obtained from Eq. 6 using the value of  $f_{\pm}$  obtained from the ODMR measurements.

$$M_z = (f_{+} + f_{-})/2 - D \quad (6)$$

Here, 2.87 GHz was used for  $D$ <sup>1,36</sup> in Eq. 6.  $M_z$  mapping in the  $\{111\}$  sector area was used to study the strain gradient in the HPHT diamond, as indicated by the red rectangle in Fig. 1d. The PL intensity image of the  $NV^-$  centre,  $T_2^*$ ,  $M_z$ , and birefringence in the  $\{111\}$  sector are compared in Supplementary Note 2. There was no obvious correlation between the imaging data. In future studies, other defect imaging methods such as X-ray topography and cathodoluminescence will be used to determine the causes of the partial distribution of the relatively low  $T_2^*$  observed in Fig. 1e. Figure 1g shows the histogram obtained from  $M_z$  spatial mapping in the  $\{111\}$  growth sector, where  $T_2^*$  mapping was performed. The solid line represents the Gaussian function fitted to the histogram. The result indicates that the diamond crystal strain was uniformly distributed throughout the HPHT diamond. The full width at half maximum (FWHM) of  $M_z$  in the Gaussian distribution, that is,  $\Delta M_z$ , was 0.06 MHz. Note that the calculated  $\Delta M_z$  includes not only in-plane variance of the strain, but also depth variance of the strain. The depth variance arises from the examined excited depth of  $\sim 400 \mu\text{m}$ . Assuming that strain is hydrostatic, the strain gradient in the depth direction of the examined HPHT diamond is expected to be comparable to that obtained by in-plane  $M_z$  imaging in this study. In future studies, the strain gradient in the depth direction should be directly observed by ODMR using a conventional confocal microscope having a depth resolution of  $1 \mu\text{m}$ . Here, the spatial dispersion of the strain related ODMR shift,  $\Delta M_z$ , induces inhomogeneous broadening of the ODMR spectrum of the  $NV^-$  centre<sup>18</sup>. Thus,  $\Delta M_z$  corresponds to the dephasing rate of the strain gradient  $1/T_2^*\{\text{strain gradient}\}$ <sup>18</sup> in the whole  $T_2^*$  spatial mapping region (Fig. 1e). The slope of the strain gradient in the  $\{111\}$  plane direction of the diamond crystal was estimated to be  $0.06 \text{MHz}/1100 \mu\text{m} = 0.05 \text{kHz} \mu\text{m}^{-1}$ . This value is approximately one order of magnitude smaller than the strain gradient of  $2.8 \text{kHz} \mu\text{m}^{-1}$  for nitrogen-doped CVD diamond with  $[N_T] = 0.75 \text{ppm}$  reported by Bauch and coworkers<sup>18</sup>. In this study, the critical synthesis parameter for improvement of homogeneity of  $T_2^*$  and strain gradient in examined HPHT diamond crystals were not clear. It is

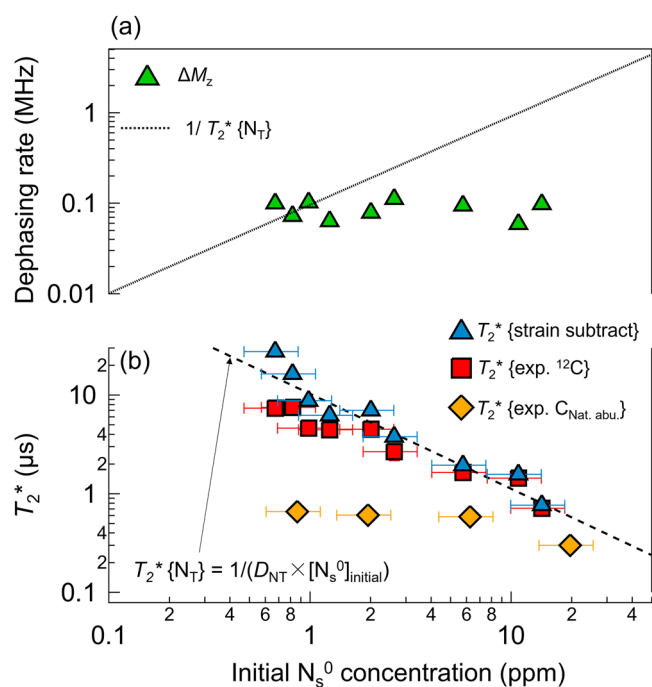


**Fig. 2 | Effect of concentration of nitrogen impurities on spin-dephasing rate.** **a** Dependence of initial neutral substitutional nitrogen concentration,  $[N_s^0]_{\text{initial}}$ , on two-spin dephasing rate component. Black dashed line and green triangles show dipole-dipole interaction (DDI) from electron-spin bath of nitrogen impurities and strain gradient in diamond crystal, respectively. **b** Dependence of initial neutral substitutional nitrogen concentration  $[N_s^0]_{\text{initial}}$  on spin-dephasing time,  $T_2^*$ . Red square, orange rhombus, and blue triangle, respectively, show experimental spin-dephasing time as  $T_2^*\{\text{exp. }^{12}\text{C}\}$  and  $T_2^*\{\text{exp. C}_{\text{Nat. Abu.}}\}$  from  $^{12}\text{C}$ -enriched and carbon natural-abundance HPHT diamond, and spin dephasing time obtained by subtracting spatial strain gradient in diamond crystal from  $T_2^*\{\text{exp. }^{12}\text{C}\}$ :  $T_2^*\{\text{strain subtract}\}$ . The black dashed line shows the dephasing time limited by DDI from the electron-spin bath of nitrogen impurities,  $T_2^*\{N_T\}$ . The vertical error bars for  $T_2^*\{\text{exp. }^{12}\text{C}\}$  and  $T_2^*\{\text{exp. C}_{\text{Nat. Abu.}}\}$  indicate the standard deviation of the Gaussian distribution. The horizontal error bars for  $T_2^*\{\text{exp. }^{12}\text{C}\}$ ,  $T_2^*\{\text{exp. C}_{\text{Nat. Abu.}}\}$  and  $T_2^*\{\text{strain subtract}\}$  indicate the EPR estimation error for initial  $N_s^0$  concentration.

possible that reducing the growth rate to  $\sim 1 \text{mg h}^{-1}$ , which is smaller than reported value<sup>29</sup>, led to the high quality of the diamond single crystal. This low growth rate may cause reduction of defects such as dislocation. In future works, an investigation of the relationship between formation of defect and various synthesis parameters such as growth rate is expected.

Here, strain gradients in diamond crystals caused by high doping with impurities such as boron and phosphorus have been reported<sup>37-39</sup>. Therefore, in the next section, the dependence of the strain gradient observed in this study on the nitrogen impurity concentration is discussed.

### Dependence of strain gradient in diamond on concentration of nitrogen impurities

The dependence of the strain gradient in diamond crystals on the concentration of nitrogen impurities was investigated. The green triangles in Fig. 2a show the relationship between  $\Delta M_z$  and  $[N_s^0]_{\text{initial}}$ . To determine the strain gradient,  $\Delta M_z$ , in-plane  $\{111\}$  spatial  $M_z$  mapping was carried out for nine  $^{12}\text{C}$ -enriched HPHT diamond crystals with different  $[N_s^0]_{\text{initial}}$ . The resulting  $\Delta M_z$  ranged from 0.06 to 0.1 MHz and did not have a strong dependence on  $[N_s^0]_{\text{initial}}$ , indicating that the strain gradient in the diamond crystal was not caused by uptake of nitrogen under the  $[N_s^0]_{\text{initial}}$  ranging from 0.7 to 14 ppm. When strain gradient is independent of nitrogen concentration, dephasing effect due to strain gradient becomes negligible when nitrogen concentration is larger, e.g., 10 ppm, leading to improvement of shot-noise limit. But, in practical sensing, as well as improving shot noise, spin manipulation with high fidelity is also one of essential key technology

for high sensitivity as explained in the introduction part. In the case of spin rotation time  $\sim 100$  ns in this study,  $T_2^*$  over  $10 \mu\text{s}$  is needed for high fidelity of spin manipulation. Therefore, the reduction of strain gradient in diamond with lower nitrogen concentration less than 1 ppm is desirable for practical sensing. The obtained strain gradient  $\Delta M_z$  ranging from 0.06 to 0.1 MHz corresponds to stress ranging from 5 to 8 MPa, assuming that the strain is hydrostatic<sup>40</sup>. Sumiya et al. reported that an Ib-diamond containing several tens to hundreds of ppm of nitrogen impurities has a larger inhomogeneous strain distribution<sup>41</sup>. This fact suggests that nitrogen-doped diamond has relatively large strain gradient. This inhomogeneous strain distribution could shift the resonance frequency of the NV<sup>-</sup> centre. Therefore, in Ib-diamond crystals, the inhomogeneous strain distribution shortens  $T_2^*$  of the NV<sup>-</sup> centre. To determine the effect of the nitrogen-impurity concentration and strain gradient on  $T_2^*$ , the spin-dephasing rates  $1/T_2^*\{N_T\}$  estimated using Eq. 4 were superimposed on Fig. 2a, as indicated by the black dotted line. As shown in Fig. 2a,  $1/T_2^*\{N_T\}$  was approximately 10 times larger than the strain-gradient dephasing rate,  $\Delta M_z$ , at  $[N_s^0]_{\text{initial}} \approx 10$  ppm. The difference between  $\Delta M_z$  and  $1/T_2^*\{N_T\}$  became smaller as  $[N_s^0]_{\text{initial}}$  decreased, and the values of both were comparable at  $[N_s^0] \approx 1$  ppm. This suggests that in the region of a relatively small  $[N_s^0]_{\text{initial}}$  ( $\sim 1$  ppm),  $T_2^*$  is expected to be governed not only by DDI from the electron-spin bath of nitrogen impurities but also by the strain gradient in the diamond crystal. To verify this  $T_2^*$  dephasing model, the relationship between the experimentally-obtained spin-dephasing time of the <sup>12</sup>C-enriched HPHT diamond crystal ( $T_2^*\{\text{exp. }^{12}\text{C}\}$ ) and  $[N_s^0]_{\text{initial}}$  was investigated. Here,  $T_2^*\{\text{exp. }^{12}\text{C}\}$ , which is plotted in Fig. 2b as red rectangles, is the median value of  $T_2^*$ ,  $\langle T_2^* \rangle$ , in a Gaussian distribution, as shown in Fig. 1f. The vertical error bars for  $T_2^*\{\text{exp. }^{12}\text{C}\}$  indicate the standard deviation of the Gaussian distribution; they are much smaller than the marker size.  $T_2^*\{\text{exp. }^{12}\text{C}\}$  decreased with increasing  $[N_s^0]_{\text{initial}}$  (Fig. 2b). This suggests that the DDI from the electron-spin bath of nitrogen impurities was significant dephasing contribution respect to the other dominant contributions including strain gradient. The  $T_2^*\{\text{exp. C}_{\text{Nat. Abu.}}\}$  data obtained from carbon natural-abundance HPHT diamond samples were plotted in the figure as orange rhombuses.  $T_2^*\{\text{exp. C}_{\text{Nat. Abu.}}\}$  also decreased with an increase in  $[N_s^0]_{\text{initial}}$ . Furthermore,  $T_2^*\{\text{exp. C}_{\text{Nat. Abu.}}\}$  became significantly smaller than  $T_2^*\{\text{exp. }^{12}\text{C}\}$  with a decrease in  $[N_s^0]_{\text{initial}}$ . This significant decrease of  $T_2^*\{\text{exp. C}_{\text{Nat. Abu.}}\}$  from  $T_2^*\{\text{exp. }^{12}\text{C}\}$  was caused by the presence of magnetic noise from the <sup>13</sup>C nuclear spin in carbon natural-abundance HPHT diamond samples. It means that <sup>12</sup>C enrichment is indispensable for obtaining  $T_2^*$  of larger than  $1 \mu\text{s}$ . The relationship between  $T_2^*\{N_T\}$  and  $[N_s^0]_{\text{initial}}$  shown in Eq. 4 is superimposed on Fig. 2b using a black dashed line. The difference between  $T_2^*\{\text{exp. }^{12}\text{C}\}$  and  $T_2^*\{N_T\}$  became significantly larger with a decrease in  $[N_s^0]_{\text{initial}}$ . As discussed above, one possible mechanism that shortens  $T_2^*\{\text{exp.}\}$  is the strain gradient of the diamond crystals. To eliminate the strain-gradient dephasing rate ( $\Delta M_z$ ) from  $1/T_2^*\{\text{exp. }^{12}\text{C}\}$ ,  $T_2^*\{\text{strain subtract}\}$  was estimated, as defined below:

$$\frac{1}{T_2^*\{\text{strain subtract}\}} \equiv \frac{1}{T_2^*\{\text{exp. }^{12}\text{C}\}} - \Delta M_z \quad (7)$$

$T_2^*\{\text{strain subtract}\}$ , which is plotted as blue triangles in Fig. 2b, had approximately the same value as  $T_2^*\{N_T\}$  (Fig. 2b), as indicated by the black dashed line, based on Eq. 4. This result shows that reducing the strain gradient extends  $T_2^*$  to a value limited by DDI from the electron-spin bath of nitrogen impurities, as shown in Eq. 8:

$$\frac{1}{T_2^*\{\text{strain subtract}\}} \sim \frac{1}{T_2^*\{N_T\}} \quad (8)$$

Reducing the strain gradient in diamond crystals is essential for further improving  $T_2^*$ , especially in the nitrogen-impurity concentration range below 1 ppm. Furthermore, reducing strain and strain gradient in the lower nitrogen impurity concentration is essential for high-performance quantum

computation and quantum telecommunication using a single NV<sup>-</sup> centre. The electronic noise from the strain shifts the ODMR frequency and zero phonon line wavelength<sup>42</sup> of a single NV<sup>-</sup> centre, and this shift causes fluctuation of the quantum state of a single NV<sup>-</sup> centre, leading to the degradation in the performance of these quantum applications. Here,  $T_2^*\{\text{strain subtract}\}$  at an  $[N_s^0]_{\text{initial}}$  of  $<1$  ppm was slightly larger than  $T_2^*\{N_T\}$ , as indicated by the black dashed line as shown in Fig. 2b.  $T_2^*\{N_T\}$  was obtained from N-doped CVD diamond crystals<sup>6,10</sup> with  $[^{13}\text{C}] \sim 500$  ppm. The dephasing rate by <sup>13</sup>C nuclear spin with  $[^{13}\text{C}] \sim 500$  ppm was  $\sim 1/20 \mu\text{s}^{-1}$  using the reported coefficient between  $[^{13}\text{C}]$  and <sup>13</sup>C dephasing rate<sup>1</sup>. This rate is significant for the NV<sup>-</sup> centre spin dephasing in diamond crystals with  $[N_s^0]_{\text{initial}}$  of less than 1 ppm. In this study, the dephasing rate by <sup>13</sup>C nuclear spin with  $[^{13}\text{C}] \sim 50$  ppm was  $\sim 1/200 \mu\text{s}^{-1}$ . The one order of magnitude higher isotopically <sup>12</sup>C enrichment may cause the observed slight elongation of  $T_2^*\{\text{strain subtract}\}$  relative to  $T_2^*\{N_T\}$  with  $[N_s^0]_{\text{initial}}$  of less than 1 ppm in Fig. 2b. Furthermore, we considered the effects of defects inherent in the CVD growth on  $T_2^*$ . Previous studies have demonstrated that nitrogen-doped CVD diamond crystals with nitrogen-impurity concentrations below 1 ppm contain various vacancy-impurity complexes<sup>43-46</sup>. To date, these defects have not been observed in nitrogen-doped HPHT diamond crystals, including those examined in this study. The non-formation of the vacancy-impurity complexes in HPHT diamond crystals may cause a slight elongation of  $T_2^*\{\text{strain subtract}\}$  from  $T_2^*\{N_T\}$  at an  $[N_s^0]_{\text{initial}}$  of  $<1$  ppm in Fig. 2b.

In conclusion, high uniformity of the  $T_2^*$  of NV<sup>-</sup> centres in millimetre-scale area was demonstrated using <sup>12</sup>C-enriched HPHT diamond crystals. The median value of  $T_2^*$ ,  $\langle T_2^* \rangle$ , for the NV<sup>-</sup> centres formed in the high-pressure, high-temperature diamond was  $4.5 \mu\text{s}$  when the nitrogen concentration in diamond crystal was 1.3 ppm. The spatial variance of  $T_2^*$  was as small as 10% over a millimetre-scale region ( $1.1 \times 1.1 \text{ mm}^2$ ) within the  $\{111\}$  growth sector with a thickness of 0.4 mm. The value of  $\langle T_2^* \rangle$  was approximately 2/3 times the value limited by the DDI from the electron-spin bath of the nitrogen impurities, suggesting that the strain gradient in the diamond crystal partially limits  $T_2^*$ . The strength of the interaction between the electron spins of the NV<sup>-</sup> centre and strain in the diamond crystal,  $M_z$ , was measured within the  $\{111\}$  growth sector, where  $T_2^*$  was estimated. The spatial variance of  $M_z$ , which corresponds to the strain gradient, was 0.06 MHz. The dephasing rate originating from the strain gradient was comparable to that originating from the electron-spin bath of nitrogen impurities. The effect of the nitrogen-impurity concentration on the strain gradient was investigated using several HPHT diamond crystals with  $[N_s^0]_{\text{initial}}$  ranging from 0.7 to 14 ppm. The strain gradient was independent on the nitrogen impurity concentration ranged in over one order of magnitude. Especially,  $T_2^*$  is limited by the electron-spin bath of nitrogen impurities with  $[N_s^0] > 2$  ppm because the dephasing rate due to the electron-spin bath of the nitrogen impurities is larger than the obtained dephasing rate of the strain gradient. On the other hand,  $T_2^*$  was limited by the strain gradient in the diamond crystals when  $[N_s^0]_{\text{initial}} < \sim 1$  ppm. Thus, reducing the strain gradient is essential for further improvement of  $T_2^*$  when the nitrogen-impurity concentration is relatively small ( $<1$  ppm), which is a requirement for achieving high-sensitivity magnetometry by NV quantum sensing.

## Methods

### Sample preparation

<sup>12</sup>C isotopically enriched HPHT synthesized diamond was examined in this study<sup>28</sup>. <sup>12</sup>C-enriched CVD polycrystalline diamond was used as the starting material (carbon source) because <sup>12</sup>C isotopically enriched graphite is not commercially available<sup>47</sup>. The reduced <sup>13</sup>C concentration was assumed to be 50 ppm. The concentration of nitrogen impurities in the examined diamonds was controlled by the amount of Ti or Al (nitrogen-getter metal) added to the solvent-metals such as Fe and Co<sup>28</sup>. Diamond single-crystals were grown on (001) plane seed crystals in Co-Ti-Cu, Fe-Co-Ti-Cu, Fe-Al, Fe-Co-Al (99.98%–99.999%, RARE METALLIC Co., Ltd.) solvents via a temperature-gradient method at 5.5 GPa in the temperature range of 1300–

1350 °C for 40–80 h. A small temperature fluctuation less than  $\pm 7.5$  °C was achieved by using cooling water in the modified belt-type, high-pressure apparatus. When Ti was added as a nitrogen getter, Cu was added to the solvent. The Cu additive suppressed the formation of Ti-C inclusion defects in the grown HPHT diamond<sup>48</sup>. The synthesised diamonds were then laser-cut parallel to the {111} plane. The spin coherence time was maximised when the external magnetic field was parallel to NV<sup>-</sup> centre's dipole-oriented axis of [111]. For NV sensing, {111} oriented diamond crystal is typically used<sup>12,49–51</sup> because the precise alignment of the external magnetic field parallel to the NV axis of [111] is easier than that of {001}, {110} oriented diamond crystal. A magnet can be arranged in a compact manner using a {111}-oriented diamond, leading to the miniaturisation of the NV sensing system<sup>49</sup>. Laser cutting caused non-diamond phase carbon such as graphite and amorphous carbon defects to form on the surfaces of the diamond samples. The amorphous carbon defect has paramagnetic properties<sup>52</sup> and could cause degradation of  $T_2^*$  of NV<sup>-</sup> centre distributed in surface of diamond crystal. After laser cutting, acid treatment ( $\text{H}_2\text{SO}_4:\text{HNO}_3 = 1:1$  at 360 °C for 2 h) was used to remove the graphite and the surface amorphous carbon from the diamond samples. The in-plane size of the cut diamonds was approximately 2 mm  $\times$  2 mm and the thickness in the [111] direction was  $400 \pm 100$   $\mu\text{m}$ . In this study, nine HPHT diamonds were laser-cut. The concentration of nitrogen impurities was then quantified for these nine diamond samples. Most of the nitrogen impurities in the diamonds synthesized by the HPHT method are in the form of neutral substitutional nitrogen ( $\text{N}_s^0$ )<sup>53</sup>. Electron paramagnetic resonance (EPR) was used to determine the concentration of NV centres and  $\text{N}_s^0$ <sup>53,54</sup>. Here, the concentration of NV<sup>-</sup> centres and  $\text{N}_s^0$  obtained by EPR were lower than those in the {111} sector because EPR was performed with HPHT diamonds containing multiple sectors, as shown in Fig. 1d. The multisector composed of not only the {111} growth sector but also contains {110} and {113} growth sectors. The  $\text{N}_s^0$  concentration in the {110} and {113} growth sectors was one order of magnitude smaller than that in the {111} growth sector<sup>32</sup>. Thus, the EPR intensity obtained from the examined multi growth sector HPHT diamonds mainly originated from  $\text{N}_s^0$  and NV<sup>-</sup> centres in the {111} growth sector. To correct the underestimation of  $[\text{N}_s^0]$  and  $[\text{NV}^-]$ , the volume of the multi-sectors (that is, the {110} and {113} growth sectors) was subtracted from the total volume of the examined HPHT diamond samples. For some HPHT diamond samples in this study, the {111} growth sector was isolated by laser cutting and  $[\text{N}_s^0]$  and  $[\text{NV}^-]$  were directly estimated. The estimated error in  $[\text{N}_s^0]$  and  $[\text{NV}^-]$  for the {111} growth sector was within  $\pm 30\%$ . Here, the concentration of the NV centres formed during the HPHT synthesis was the detection limit for the EPR measurements in the examined HPHT diamond samples. In HPHT synthesis, the formation of vacancies is less likely to occur than in CVD synthesis. In the CVD synthesis, NV and NVH centres were typically observed<sup>54,55</sup>. The concentration of neutral substitutional nitrogen,  $[\text{N}_s^0]_{\text{initial}}$ , before formation of the NV centres in these crystals ranged from 0.7 to 14 ppm. Electron-beam irradiation followed by post-annealing (1000 °C 2 h) was carried out to form NV centres in the examined diamond<sup>54</sup>. The examined fluence was ranged from  $1 \times 10^{17}$  to  $5 \times 10^{17}$  e cm<sup>-2</sup>. The concentrations of NV<sup>-</sup> centres formed by this post-process ranged from 0.1 to 2 ppm. The obtained maximum conversion efficiency  $[\text{NV}^-]/[\text{N}_s^0]_{\text{initial}}$  was approximately 20% in this study. The ideal conversion efficiency is 50%<sup>16,17</sup>. By using electron-beam irradiation during high-temperature annealing, the best reported conversion efficiency of 45% was obtained for the Ib-diamond sample with  $[\text{N}_s^0]_{\text{initial}} = 100$  ppm<sup>16,17</sup>. The enhancement of conversion efficiency has been investigated with only over nitrogen concentration of 30 ppm<sup>56</sup>. In future work, in diamond samples with nitrogen concentrations less than 1 ppm, the conversion efficiency is expected to be enhanced by electron-beam irradiation during high-temperature annealing.

### Experimental setup

Free induction decay measurements were conducted using a home-built PL system with a pulsed microwave module (Synth NV PRO; Windfreak Technologies, LLC/arbitrary waveform generator M3202A; Keysight Inc.).

A 532 nm laser (gem 532; Laser Quantum Inc.) was pulsed using an acoustic-optic modulator (#35 250-0.2-0.53-XQ; Gooch & Housego). Red fluorescence emitted from the NV<sup>-</sup> centre by pulsed green laser excitation was collected using an achromatic lens (AC254-030-AB-ML; Thorlabs, Inc.) and detected using an avalanche photodiode (APD410A/M; Thorlabs, Inc.).

### PL intensity of NV<sup>-</sup> centres in multi-growth sectors

Here, we additionally explained the relationship between PL intensity and growth sectors as indicated in Fig. 1d-ii, iii.

The PL intensity distributed around the three triangular vertices indicated as Fig. 1d-ii is over one order of magnitude lower than that in the {111} growth sector indicated as Fig. 1d-i, indicating that the three triangular vertex areas was corresponding to the {113} or {110} sectors. It has been reported that the nitrogen density in the {113} and {110} growth sector is one order of magnitude lower than that in the {111} growth sectors<sup>32</sup>. The tapered area indicated as Fig. 1d-iii is {110} or {113} growth sector as following general HPHT diamond text. But PL intensity distributed in the tapered area was comparable to or slightly larger than {111} growth sector in Fig. 1d-i. The PL intensity in the tapered area was not corresponding to typical variation of uptake of nitrogen impurities between multi-sectors. This controversial result in this study was caused by the excitation laser reflecting and refracting at the tapered area. The laser reflecting and refracting at the tapered area, entered a {111} growth sector in central area, and the PL emission from the {111} growth sector returned to the entry-pass and was subsequently detected.

### Data availability

The datasets generated during and/or analysed in this study are available from the corresponding authors upon reasonable request.

### Code availability

The codes used for this study are available from the corresponding authors upon reasonable request.

Received: 3 April 2024; Accepted: 14 March 2025;

Published online: 08 April 2025

### References

- Barry, J. F. et al. Sensitivity optimization for NV-diamond magnetometry. *Rev. Mod. Phys.* **92**, 015004 (2020).
- Kubo, Y. et al. Hybrid quantum circuit with a superconducting qubit coupled to a spin ensemble. *Phys. Rev. Lett.* **107**, 220501 (2011).
- Gottscholl, A. et al. Spin defects in hBN as promising temperature, pressure and magnetic field quantum sensors. *Nat. Commun.* **12**, 4480 (2021).
- Castelletto, S. et al. Quantum systems in silicon carbide for sensing applications. *Rep. Prog. Phys.* **87**, 01401 (2023).
- Barry, J. F. et al. Sensitive ac and dc Magnetometry with nitrogen-vacancy-center ensembles in diamond. *Phys. Rev. Appl.* **22**, 044069 (2024).
- Edmonds, A. M. et al. Characterisation of CVD diamond with high concentrations of nitrogen for magnetic-field sensing applications. *Mater. Quantum Technol.* **1**, 025001 (2021).
- Mizuochi, N. et al. Coherence of single spins coupled to a nuclear spin bath of varying density. *Phys. Rev. B* **80**, 041201 (2009).
- Teraji, T. High-quality and high-purity homoepitaxial diamond (100) film growth under high oxygen concentration condition. *J. Appl. Phys.* **118**, 115304 (2015).
- Nakamura, K. et al. Single-crystal synthesis of highly thermal conductive <sup>12</sup>C-enriched diamond from pyrolytic carbon powder by the high-pressure, high-temperature method. *Diam. Relat. Mater.* **16**, 1765–1769 (2007).
- Bauch, E. et al. Decoherence of ensembles of nitrogen-vacancy centers in diamond. *Phys. Rev. B* **102**, 134210 (2020).

11. Balasubramanian, G. et al. Ultralong spin coherence time in isotopically engineered diamond. *Nat. Mater.* **8**, 383–387 (2009).
12. Sekiguchi, N. et al. Diamond quantum magnetometer with dc sensitivity of sub-10 pT Hz<sup>-1/2</sup> toward measurement of biomagnetic field. *Phys. Rev. Appl.* **21**, 064010 (2024).
13. Arai, K. et al. Millimetre-scale magnetocardiography of living rats with thoracotomy. *Commun. Phys.* **5**, 1–10 (2022).
14. Kehayias, P. et al. Imaging crystal stress in diamond using ensembles of nitrogen-vacancy centers. *Phys. Rev. B* **100**, 174103 (2019).
15. Aslam, N. et al. Quantum sensors for biomedical applications. *Nat. Rev. Phys.* **5**, 157–169 (2023).
16. Choi, J. et al. Depolarization Dynamics in a Strongly Interacting Solid-State Spin Ensemble. *Phys. Rev. Lett.* **118**, 093601 (2017).
17. Choi, S. et al. Observation of discrete time-crystalline order in a disordered dipolar many-body system. *Nature* **543**, 221–225 (2017).
18. Bauch, E. et al. Ultralong Dephasing Times in Solid-State Spin Ensembles via Quantum Control. *Phys. Rev. X* **8**, 031025 (2018).
19. Le Sage, D. et al. Efficient photon detection from color centers in a diamond optical waveguide. *Phys. Rev. B* **85**, 121202 (2012).
20. Wolf, T. et al. Subpicotesla diamond magnetometry. *Phys. Rev. X* **5**, 041001 (2015).
21. Yoneda, J. et al. A quantum-dot spin qubit with coherence limited by charge noise and fidelity higher than 99.9%. *Nat. Nanotechnol.* **13**, 102–106 (2018).
22. Masuyama, Y. et al. Extending coherence time of macro-scale diamond magnetometer by dynamical decoupling with coplanar waveguide resonator. *Rev. Sci. Instrum.* **89**, 125007 (2018).
23. Masuyama, Y. et al. Columnar excitation fluorescence microscope for accurate evaluation of quantum properties of color centers in bulk materials. *Sci. Rep.* **14**, 18135 (2024).
24. Wang, P. et al. High-resolution vector microwave magnetometry based on solid-state spins in diamond. *Nat. Commun.* **6**, 6631 (2015).
25. Friel, I. et al. Control of surface and bulk crystalline quality in single crystal diamond grown by chemical vapour deposition. *Diam. Relat. Mater.* **18**, 808–815 (2009).
26. Sumiya, H. & Tamasaku, K. Large Defect-Free Synthetic Type IIa Diamond Crystals Synthesized via High Pressure and High Temperature. *Jpn. J. Appl. Phys.* **51**, 090102 (2012).
27. Burns, R. C. et al. HPHT growth and x-ray characterization of high-quality type IIa diamond. *J. Phys. Condens. Matter* **21**, 364224 (2009).
28. Miyakawa, M. et al. Nitrogen concentration control in diamonds grown in Co-(Fe)-Ti/Al solvents under high-pressure and high-temperature. *Jpn. J. Appl. Phys.* **61**, 045507 (2022).
29. Sumiya, H. et al. Growth rate of high-quality large diamond crystals. *J. Cryst. Growth* **237–239**, 1281–1285 (2002).
30. Kanda, H. et al. Surface structures of synthetic diamonds. *J. Mater. Sci.* **15**, 2743–2748 (1980).
31. Kanda, H. Large diamonds grown at high pressure conditions. *Braz. J. Phys.* **30**, 482–489 (2000).
32. Burns, R. C. et al. Growth-sector dependence of optical features in large synthetic diamonds. *J. Cryst. Growth* **104**, 257–279 (1990).
33. Sangtawesin, S. et al. Origins of Diamond Surface Noise Probed by Correlating Single-Spin Measurements with Surface Spectroscopy. *Phys. Rev. X* **9**, 031052 (2019).
34. Hart, C. A. et al. N-V-Diamond Magnetic Microscopy using a Double Quantum 4-Ramsey Protocol. *Phys. Rev. Appl.* **15**, 044020 (2021).
35. Tsuji, T. et al. Extending spin dephasing time of perfectly aligned nitrogen-vacancy centers by mitigating stress distribution on highly misoriented chemical-vapor-deposition Diamond. *Adv. Quantum Technol.* **7**, 2300194 (2024).
36. Loubser, J. et al. Electron spin resonance in the study of diamond. *Rep. Prog. Phys.* **41**, 1201–1248 (1978).
37. Wojewoda, T. et al. Doping-induced anisotropic lattice strain in homoepitaxial heavily boron-doped diamond. *Diam. Relat. Mater.* **17**, 1302–1306 (2008).
38. Mermoux, M. et al. Characterization of <111> diamond thin films by micro-Raman spectroscopy. *Diam. Relat. Mater.* **13**, 886–890 (2004).
39. Shinei, C. et al. Nearly degenerate ground state of phosphorus donor in diamond. *Phys. Rev. Mater.* **4**, 024603 (2020).
40. Barson, M. S. J. et al. Nanomechanical Sensing Using Spins in Diamond. *Nano Lett.* **17**, 1496–1503 (2017).
41. Sumiya, H. et al. Distribution of internal strain and fracture strength in various single-crystal diamonds. *Diam. Relat. Mater.* **134**, 109781 (2023).
42. Alaerts, L. et al. First-principles study of the Stark shift effect on the zero-phonon line of the NV center in diamond. *Phys. Rev. Mater.* **8**, 106201 (2024).
43. Coxon, D. J. L. et al. An Ultrafast Shakedown Reveals the Energy Landscape, Relaxation Dynamics, and Concentration of the N<sub>3</sub>VH<sup>0</sup> Defect in Diamond. *J. Phys. Chem. Lett.* **11**, 6677–6683 (2020).
44. Glover, C. et al. Hydrogen incorporation in diamond: The nitrogen-vacancy-hydrogen complex. *Phys. Rev. Lett.* **90**, 185507 (2003).
45. Green, B. L. et al. Electron paramagnetic resonance of the N<sub>2</sub>V<sup>-</sup> defect in <sup>15</sup>N-Doped synthetic diamond. *Phys. Rev. B* **92**, 165204 (2015).
46. Glover, C. et al. Hydrogen Incorporation in Diamond: The vacancy-hydrogen complex. *Phys. Rev. Lett.* **92**, 135502 (2004).
47. Teraji, T. et al. Effective Use of Source Gas for Diamond Growth with Isotopic Enrichment. *Appl. Phys. Express* **6**, 055601 (2013).
48. Sumiya, H. & Satoh, S. High-pressure synthesis of high-purity diamond crystal. *Diam. Relat. Mater.* **5**, 1359–1365 (1996).
49. Kainuma, Y. et al. Compact and Stable Diamond Quantum Sensors for Wide Applications. *Adv. Quantum Technol.* **7**, 2300456 (2024).
50. Hatano, Y. et al. Transverse magnetic field effects on diamond quantum sensor for EV battery monitor. *Front. Quantum Sci. Technol.* **3**, 1432096 (2024).
51. Kubota, K. et al. Wide temperature operation of diamond quantum sensor for electric vehicle battery monitoring. *Diam. Relat. Mater.* **135**, 109853 (2023).
52. Show, Y. et al. Structural characterization of CVD diamond films using the ESR method. *Thin Solid Films* **274**, 50–54 (1996).
53. Shinei, C. et al. Equilibrium charge state of NV centers in diamond. *Appl. Phys. Lett.* **119**, 254001 (2021).
54. Shinei, C. et al. Nitrogen related paramagnetic defects: Decoherence source of ensemble of NV<sup>-</sup> center. *J. Appl. Phys.* **132**, 214402 (2022).
55. Teraji, T. & Shinei, C. Nitrogen-related point defects in homoepitaxial diamond (001) freestanding single crystals. *J. Appl. Phys.* **133**, 165101 (2023).
56. Capelli, M. et al. Increased nitrogen-vacancy centre creation yield in diamond through electron beam irradiation at high temperature. *Carbon* **143**, 714–719 (2019).

## Acknowledgements

This work was supported by MEXT Q-LEAP (JPMXS0118068379 and JPMXS0118067395). T. Teraji acknowledges the support of, JST CREST (JPMJCR1773), MIC R&D for construction of a global quantum cryptography network (JPMI00316), JSPS KAKENHI (Nos. 20H02187, 20H05661, and 19H02617), and JST Moonshot R&D (JPMJMS2062).

## Author contributions

C.S. performed the experiments on the NV centres, assisted by M.Y., H.A., M.M., T.O. and T.T. (Takashi Taniguchi). M.M. and T.T. (Takashi Taniguchi) grew the HPHT diamond samples. H.A. and T.O. carried out electron beam irradiation to form the NV<sup>-</sup> centres. M.Y. primarily designed and examined the optical setup. C.S. performed the data analysis and conceived the supplementary information. T.T. (Tokuyuki Teraji) supervised this study. C.S. and T.T. (Tokuyuki Teraji) wrote the manuscript, and all authors discussed it.

## Competing interests

The authors declare no competing interests.

## Additional information

**Supplementary information** The online version contains supplementary material available at <https://doi.org/10.1038/s43246-025-00782-7>.

**Correspondence** and requests for materials should be addressed to Chikara Shinei or Tokuyuki Teraji.

**Peer review information** *Communications Materials* thanks Wei Liu, Christian Giese and the other, anonymous, reviewer(s) for their contribution to the peer review of this work. Primary Handling Editors: Sunkook Kim and Aldo Isidori. A peer review file is available.

**Reprints and permissions information** is available at <http://www.nature.com/reprints>

**Publisher's note** Springer Nature remains neutral with regard to jurisdictional claims in published maps and institutional affiliations.

**Open Access** This article is licensed under a Creative Commons Attribution-NonCommercial-NoDerivatives 4.0 International License, which permits any non-commercial use, sharing, distribution and reproduction in any medium or format, as long as you give appropriate credit to the original author(s) and the source, provide a link to the Creative Commons licence, and indicate if you modified the licensed material. You do not have permission under this licence to share adapted material derived from this article or parts of it. The images or other third party material in this article are included in the article's Creative Commons licence, unless indicated otherwise in a credit line to the material. If material is not included in the article's Creative Commons licence and your intended use is not permitted by statutory regulation or exceeds the permitted use, you will need to obtain permission directly from the copyright holder. To view a copy of this licence, visit <http://creativecommons.org/licenses/by-nc-nd/4.0/>.

© The Author(s) 2025